THE JOURNAL OF PHYSICAL CHEMISTRY C
A JOURNAL OF THE AMERICAN CHEMICAL SOCIETY

pubs.acs.org/JPCC

Article

Structural Control of Electrodeposited Sb Anodes through Solution Additives and Their Influence on Electrochemical Performance in Na-Ion Batteries

Published as part of The Journal of Physical Chemistry virtual special issue "Esther Sans Takeuchi Festschrift".

Kelly Nieto, Daniel S. Windsor, Amanda R. Kale, Jessica R. Gallawa, Dylan A. Medina, and Amy L. Prieto*

Cite This: *J. Phys. Chem. C* 2023, 127, 12415−12427

Read Online

ACCESS | Metrics & More | Article Recommendations | Supporting Information

ABSTRACT: Alloy-based materials such as antimony (Sb) are of interest for both Li/Na-ion batteries due to their high theoretical capacity and electronic conductivity. Of the various ways to fabricate Sb films (slurry casting, sputtering, etc.) one promising route is through electrodeposition. Electrodeposition is an industrially relevant synthetic technique that allows for the use of solution additives to control different characteristics such as film uniformity, morphology, and electrical conductivity. Solution additives such as cetyltrimethylammonium bromide (CTAB) and bis(3-sulfopropyl) disulfide (SPS) have been used to control different characteristics such as particle morphology and electrical conductivity in various electrodeposits but have not been applied to the electrodeposition of Sb for battery applications. In this study, Sb films were electrodeposited with varied concentrations of CTAB and SPS and the structure, morphology, composition, and electrochemical performance in Na-ion batteries were compared. We report that CTAB and SPS additives can significantly influence electrodeposited Sb films by altering the morphology and reduce the crystallinity, affecting the electrochemical performance. These studies provide valuable insight into the tunability of alloy-based films through electrodeposition and solution additives for battery applications.

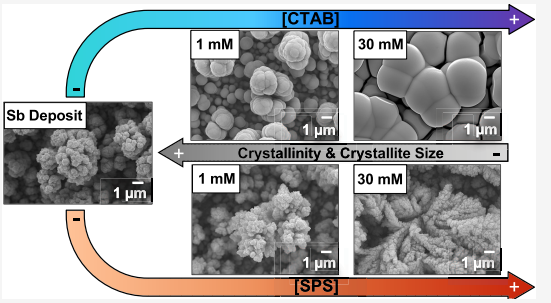

INTRODUCTION

Antimony (Sb) anodes for both sodium-ion and lithium-ion batteries have been extensively studied due to its high theoretical capacity (660 mAh/g) and electronic conductivity.[1−3] Studies have reported high reversible capacities and have implemented the use of conductive additives[4−6] and nanostructuring[7,8] to overcome issues related to mechanical stability, induced by volume expansion that occurs when Sb alloys with either sodium or lithium. To test and optimize the properties and performance of Sb, a variety of synthetic and fabrication techniques have been utilized. Traditionally, Sb thin films have been fabricated through slurry casting that consists of ball milling Sb powder, a conductive carbon additive, and a polymeric binder. Through this technique, various factors can be controlled, such as the strength of the polymeric binder, that helps maintain the mechanical integrity of the film, and the conductive additive that can improve electronic conductivity.[9−11] Other fabrication techniques used to study the properties and performance of Sb involve sputtering of Sb[12,13] and solvothermal methods,[14,15] but these techniques fall short due to cost and poor scalability.

A less prevalent technique previously reported by our group utilizes electrodeposition to synthesize Sb based anodes.[4,16−19] Through electrodeposition, Sb ions are plated electrochemically from solution onto a charged substrate.[20,21] This technique does not require binders and additives, which are necessary in slurry casted films, and vastly simplifies the understanding of the inherent properties of Sb anodes by removing the need to deconvolute the role of binders and additives.[22] In addition, electrodeposition has been found to be a valuable technique to control composition, film thickness, crystallinity, and morphology of the deposited metal.[7,23−26] This control can be accomplished by a multitude of experimental parameters (temperature, bath composition, current density, etc.) as well as the use of different solution additives.[27]

The electrodeposition of Sb has been reported in several publications using a variety of electrolyte composi-

Received: February 16, 2023
Revised: June 1, 2023
Published: June 27, 2023

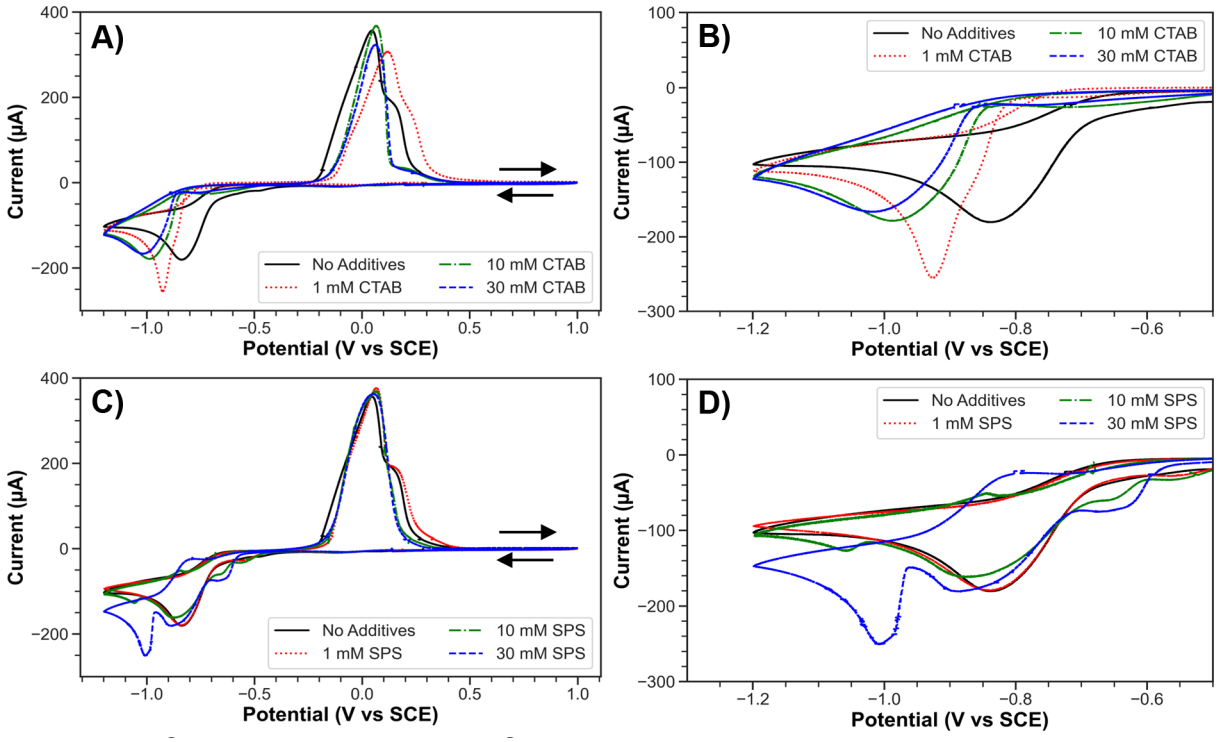

Figure 1. Cyclic voltammetry of the Sb deposition solution with varying concentrations of CTAB (A and B) and SPS (C and D). Panels B and D are magnifications of the redox events from −1.2 V to −0.5 V vs SCE.

tions.[22,25,28−30] Commonly used electrodeposition baths consist of acidic aqueous solutions with an Sb precursor ($SbCl_3$, Sb_2O_3, etc.) and various organic additives (tartaric acid, citric acid, etc.) to aid with the complexation of Sb(III).[28,29,31,32] To successfully plate Sb, additives are needed to help improve the stability and solubility of Sb(III); otherwise, the deposition proceeds at higher voltages and with slow kinetics due to the formation of oxides in solution.[29,33] By tuning the bath composition, studies have shown successful control over the deposition and growth of Sb to form films with desirable properties.[26,30,34]

In combination with the complexing agent, alternative organic compounds have been implemented to control grain refinement and leveling of the deposition.[35] These additives can be known as levelers or brighteners.[27] A leveler is defined as an additive that fills pits in the electrode surface and promotes the deposition of a smooth surface.[36] A brightener can inhibit the rate of the electrodeposition by interacting with the electrode surface and preventing the deposition of the active ion in that area.[37] As a result, brighteners can also help level the micro profile of the electrode surface without the need for polishing after the deposition.[27,37] Additives, such as bis(3-sulfopropyl) disulfide (SPS) that acts a brightner,[38−40] and sodium gluconate,[41,42] are typically used in copper and nickel plating baths, respectively, and an extensive library of additives have been investigated for other metal depositions.[36,43,44] Surfactants, such as cetyltrimethylammonium bromide (CTAB), have also been used in deposition baths due to their potential to affect the surface tension between the electrolyte and the electrode and can have effects on coating adhesiveness and morphology at varying concentrations.[45,46] Depending on the interactions of CTAB with the substrate or the active metal being deposited, it may act as a leveling or brightening agent.[47−49] Additonally, CTAB can interact directly with the deposited metal instead of the substrate and has been used to cap the growth of particles as demonstrated in nanoparticle synthesis[50−52] and also has the potential to act as a corrosion inhibitor.[53] Despite the tunability that can be acheived through these organic additives, there are few publications reporting the tunability of electrodeposited Sb anodes for battery applications using solution additives.[7,54]

Herein we report the effect of solution additives, such as CTAB and SPS, on the electrodeposition of Sb anodes in aqueous-based electrolyte baths and the subsequent impacts on the electrodes electrochemical performance in a sodium-ion battery (NIB). We report that both CTAB and SPS can dramatically influence the morphology and crystallinity of the deposited films. These effects are magnified with the increase in concentration of the additive and allows for the tunability of crystallinity and morphology, which impacts the electrochemical performance of these Sb films. In particular, the films deposited with CTAB have more stable cycling due to mechanical robustness, whereas the films deposited with SPS have improved rate capabilities for Na-ion battery applications.

METHODS

Electrodeposition Solution of Sb. The base electrodeposition solution of Sb has been described in previous work and consists of 200 mM sodium gluconate (Sigma, ACS reagent), and 30 mM antimony trichloride ($SbCl_3$, Sigma-Aldrich, anhydrous >99.0%) in 100 mL of Millipore (>15 MΩ·cm) water.[22] Solution additives were added in a variety of concentrations (1 mM, 10 mM, 30 mM) for (1-hexadecyl)-trimethylammonium bromide (CTAB, 98%, Alfa Aesar) and bis(sodium sulfoproply)-disulfide (SPS, 98.9%, CHEM-IMPEX). In addition, a mixed solution containing both CTAB and SPS was made using the base solution and a concentration of 30 mM CTAB and 30 mM SPS.

https://doi.org/10.1021/acs.jpcc.3c01086
J. Phys. Chem. C 2023, 127, 12415−12427

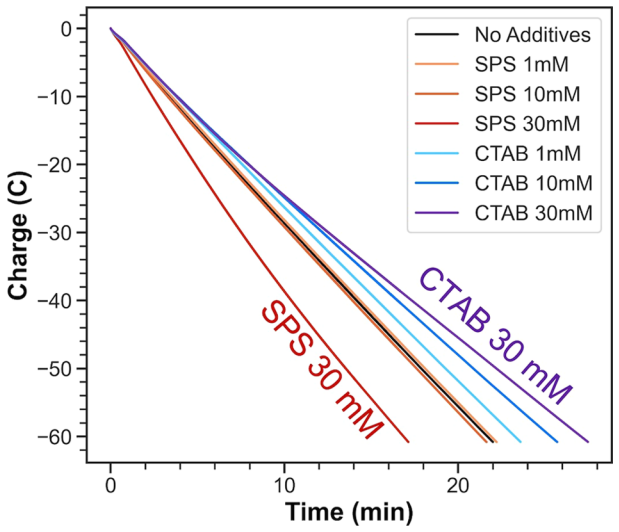

Figure 2. Summary of chronocoulometry data of the Sb electrodepositions with different concentrations of CTAB and SPS. Depositions were done using chronocoulometry and the charge limit was set to −60 C.

For the electrodeposition solutions, sodium gluconate was stirred in a beaker containing 100 mL of Millipore (>15 MΩ·cm) water for ∼5 min. Then either CTAB or SPS was added with a concentration of 1 mM, 10 mM, or 30 mM and was stirred until the additive was dissolved. To finish the solution, 30 mM $SbCl_3$ was added to the solution and sonicated (Cole-Parmer, 08895-01) until a colorless homogeneous mixture was formed.

Electrochemical Characterization of Deposition Solutions. Cyclic voltammetry (CV) was used to characterize the deposition solutions with a Gamry Reference 3000 potentiostat and determine the reduction potential at which to deposit Sb. The CVs were taken in a three-electrode setup consisting of a saturated calomel electrode (SCE) as the reference, a platinum mesh counter electrode, and a platinum disk working electrode at a scan rate of 50 mV/s unless otherwise noted.

Electrodeposition of Sb. The Sb thin film electrodes were electrodeposited using a Gamry Interface 1010E potentiostat and an in-house apparatus described in previous studies.[22] A four-inch square of textured Cu foil (tCu, Oak-Mitsui, TLB-DS Cu foil) was washed with a concentrated H_3PO_4 solution for 30 s to remove surface oxides, followed by Millipore water and ethanol wash to remove excess acid and water on the surface of the film. The electrochemical set up consisted of a tCu working electrode, a stainless-steel mesh as the counter electrode, and an SCE as the reference. Using chronocoulometry, a constant negative potential of −1.05 V vs SCE was applied and the charge limit was set to 3 C/cm^2. The deposited film was then rinsed with Millipore water and absolute ethanol to remove the remaining deposition solution.

Electrolyte Preparation, Cell Assembly, and Galvanostatic Cycling. All cell assembly and electrolyte preparation was done in an argon filled glovebox (O_2 < 1 ppm, H_2O < 0.5 ppm). The electrolyte used for all experiments consisted of a 1 M solution of sodium perchlorate ($NaClO_4$, Sigma-Aldrich, ≥98% ACS reagent) with an addition of 5% by volume fluoroethylene carbonate (FEC, Sigma-Aldrich, 99%) in a base electrolyte solution containing polyethylene carbonate (PC, Sigma-Aldrich, 99.7%).

To test the electrochemical performance of the deposited Sb films, half-cells were assembled in two electrode Swageloks. The electrodeposited film was cut into circular 1/2″ in diameter punches and were massed out to acquire the amount of the active material. The thin films were used as the working electrode, and a polypropylene separator (MTI Corp), followed by a Whatman glass filter, and another polypropylene separator were used as the separator stack. An excess amount of electrolyte, ∼200 μL, was placed in the cell after the separators. Na metal (Aldrich, cubes in mineral oil, 99.9%) was

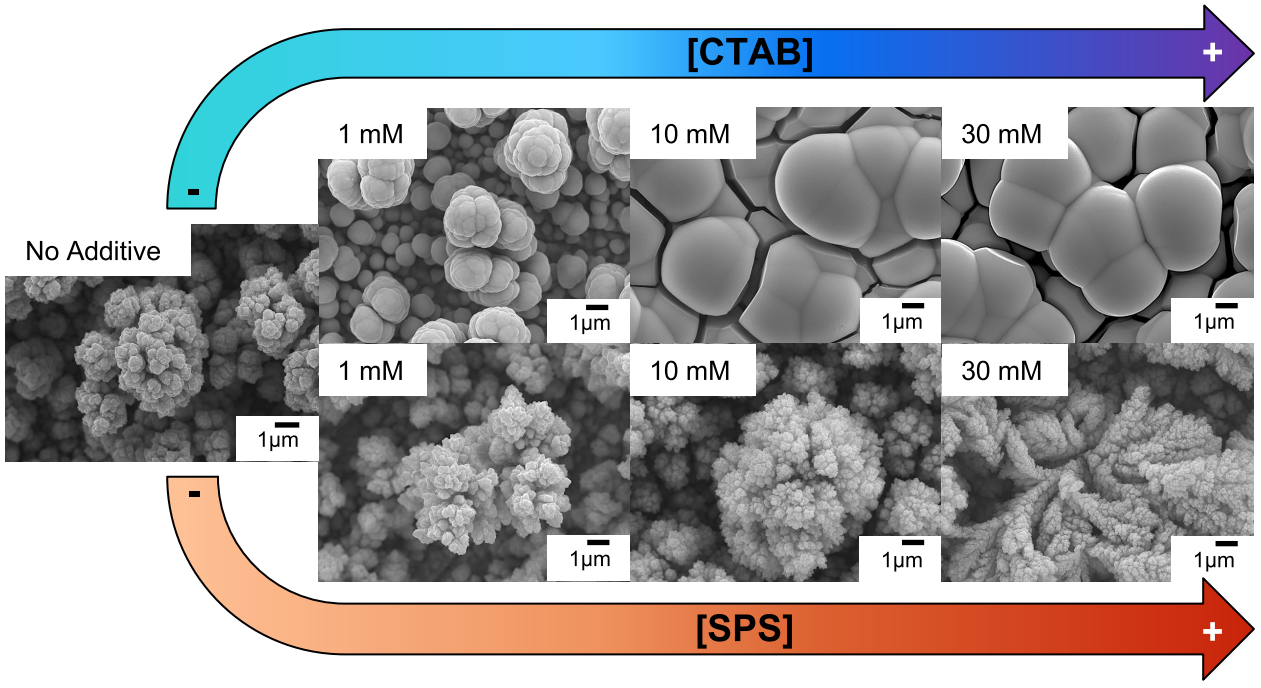

Figure 3. SEM images of Sb films deposited with no additive (left) and different concentrations of CTAB (top) and SPS (bottom).

https://doi.org/10.1021/acs.jpcc.3c01086
J. Phys. Chem. C 2023, 127, 12415−12427

then rolled out with a Teflon roller with hexanes, cleaned with an extra soft child's toothbrush, and was punched into a 1/2″ circular punch. Pressure was then applied through the SS rod, spring, Cu rod to make sure that all parts were in contact in the Swagelok cell.

Once assembled, the Na-ion half-cells were cycled with an Arbin battery tester (LBT-20084). The cells were allowed to rest for 12 h after assembly and were galvanostatically cycled at a rate of C/2, unless noted otherwise, with calculated current densities based on the mass of active material. The voltage range at which the cells were cycled was 0.01 V−1.5 V vs Na/Na^+ unless otherwise noted. Cycling performance was analyzed and graphed with a Python code using the NumPy and Pandas packages.

Electrochemical Characterization of Sb Electrodes. Cyclic voltammetry experiments on a polished copper rod, 30 mM CTAB, 30 mM SPS, and no additive Sb films were done using a three-electrode Swagelok cell in the potential window of 2 V−2.6 V vs Na/Na^+ at scan rates of 50 mV/s, 100 mV/s, 150 mV/s, 200 mV/s, and 250 mV/s. The Sb electrode acted as the working electrode, sodium metal was used as the counter and reference electrode, and a 1 M $NaClO_4$ in PC with 5% FEC by volume solution was used as the electrolyte. Electrochemical impedance spectroscopy (EIS) experiments were conducted on sodium half-cells using a Gamry Interface 1010E potentiostat. Experiments were conducted at room temperature at open circuit potential (OCP) once the cells rested for 12 h to allow for the cells to equilibrate and reach a stable OCP. A constant AC voltage of 10 mV rms and EIS was carried out over a frequency range of 0.1 to 100,000 Hz.

Materials Characterization. The surface morphology of electrodeposited films was analyzed with Scanning Electron Microscopy (SEM) using a JEOL JSM-6500F Microscope at 15 kV. X-ray Photoelectron Spectroscopy was performed with a Physical Electronics (PHI) 5800 series Multi-Technique ESCA system with a monochromatic Al Kα ($h\nu$ = 1486.6 eV) X-ray source operating at 350.0 W. Sputtering with an Ar^+ ion gun was performed at 5 keV for time increments of 30 s, and data were worked up using CasaXPS software.[55] Briefly, a GL(0) line shape was used with defined spin-splitting energy differences from reference spectra.[56,57] For p-orbital splitting, peak areas were defined to be 1:2 for $p_{1/2}$ and $p_{3/2}$, respectively, and d-orbital peak areas were defined to be 2:3 for $d_{3/2}$ and $d_{5/2}$ peaks, respectively. A Shirley background was used for all high-resolution spectra, and binding energies were calibrated with adventitious carbon at 285.0 eV.

Additional structural characterization was done through powder X-ray Diffraction (PXRD) with a Bruker D8 Discover DaVinci powder X-ray diffractometer using Cu Kα radiation and a 0.2 mm slit opening. Rietveld refinements were performed using Topas v6 (Bruker AXS). Peak profiles were fit using a double-Voigt approach. Preferred orientation was modeled using the March-Dollase model for the (1 0 $\bar{2}$) and (2 $\bar{1}$ 0). Further discussion on how the refinements were done can be found in the Supporting Information.

RESULTS AND DISCUSSION

Influences of Solution Additives on the Electrodeposition of Sb. To identify events occurring during deposition, cyclic voltammetry (CV) was performed on the various deposition solutions. In our solutions, $SbCl_3$ is readily dissolved into an aqueous solution containing sodium gluconate, where sodium gluconate is believed to behave as a complexing agent.[58] This complexation aids in dissolving $SbCl_3$ and helps prevent the oxidation of Sb. Through cyclic voltammetry, seen in Figure 1A−D, the solution containing only $SbCl_3$ and sodium gluconate is found to only have one significant reduction event at about −0.85 V vs SCE, associated with the reduction of $Sb^{3+} + 3e^- \rightarrow Sb^0$. The large oxidation event at 0 V vs SCE is associated with the oxidation of Sb^0 back to Sb^{3+}. Upon the addition of CTAB, Figure 1A and B, the Sb reduction peak is shifted to more negative reduction potentials that are indicative of adsorption onto the surface of the electrode, or suppression of the rate of deposition of Sb. When increasing the concentration of CTAB beyond 10 mM, the reduction of Sb does not shift further and remains at 1 V vs SCE. Interestingly, when CTAB is used in solution, the time it takes to reach the charge limit set for the chronocoulometry deposition increases, Figure 2. As the concentration is increased to 30 mM, it takes an additional 6 min to reach the charge limit and further leads us to believe that CTAB is suppressing or slowing down the rate of Sb deposition.

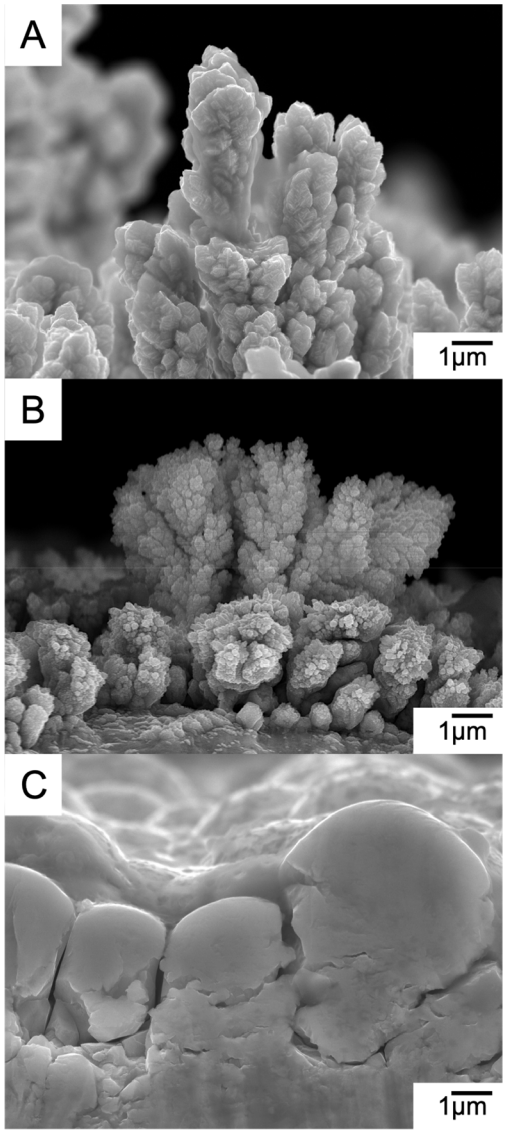

Figure 4. Cross section SEM images of the Sb deposited with (A) no additive, (B) SPS 30 mM, and (C) CTAB 30 mM.

https://doi.org/10.1021/acs.jpcc.3c01086
J. Phys. Chem. C 2023, 127, 12415−12427

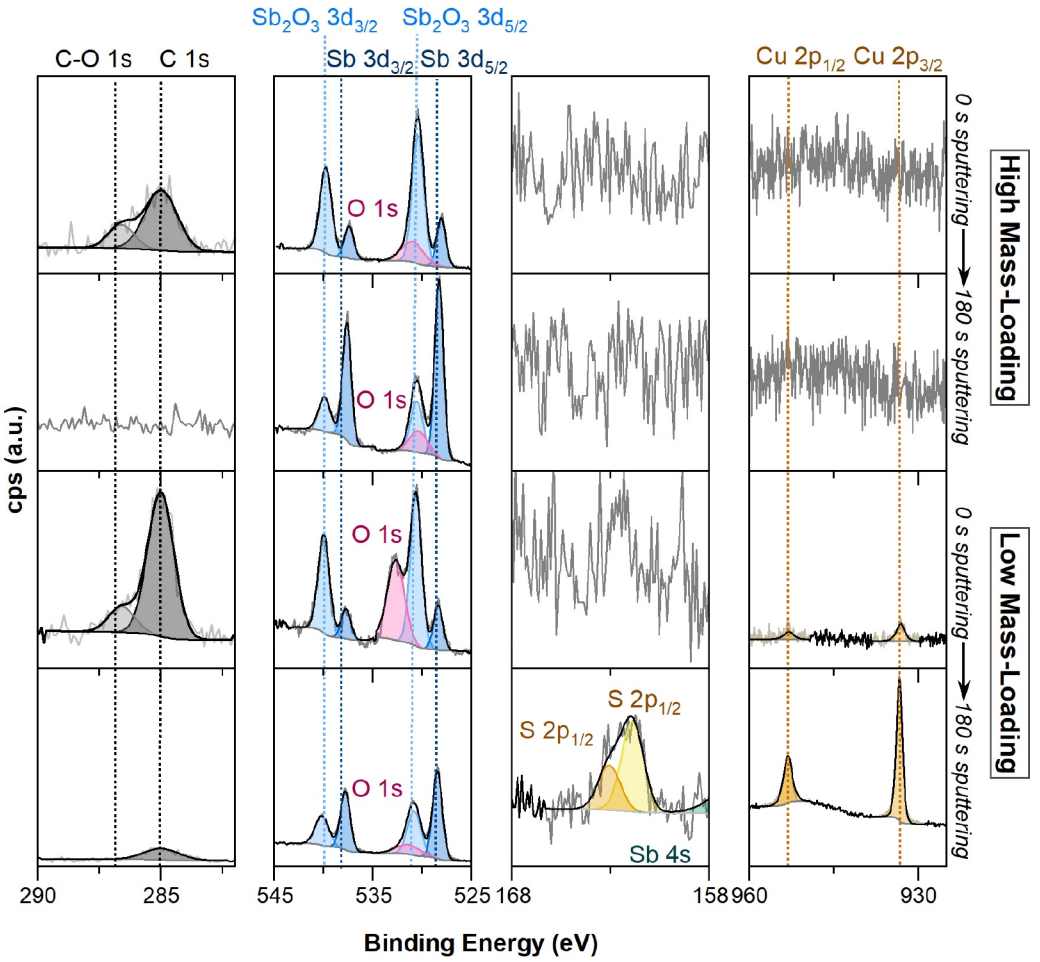

Figure 5. High-resolution X-ray photoelectron spectra of Sb electrodeposited on copper with SPS. Carbon, antimony, sulfur, and copper regions are displayed for the full chronocoulometric electrodeposition (high mass-loading) and the 30 s chronoamperometric electrodeposition (low mass-loading), both at pristine conditions and after sputtering for 3 min. Equivalent XPS analysis was done on the 30 mM CTAB film and can be found in Figure S2 and Figure S3.

When using SPS as the additive, Figure 1C and D, the main reduction peak associated with Sb does not shift to overpotentials, but additional reduction events appear. These reduction events are believed to be related to the complexation of Sb with SPS, as no redox events are seen when SPS is the only species present in solution, Figure S1. The smaller reduction events could be attributed to fouling of the electrode and disruption of the deposition of Sb as they are not present in the first scan of the CV, Figure S1. In addition, when SPS is included in the deposition solution it appears to act as an accelerant for the deposition of Sb as seen in Figure 2. However, this effect only seems to be substantial in the 30 mM SPS solution, and lower concentrations of SPS have minimal effects. This behavior has been observed in the work of Moffat et al., where SPS was found to displace the passivating layer at the copper surface that consisted of Cl^- and poly(ethylene glycol).[59] Displacement occurs because of the preferential adsorption of short chained disulfide or thiol groups in SPS onto the surface of the copper substrate and a high concentration is needed to have a significant effect on displacing the passivating layer.[59]

Structural Characterization of Electrodeposited Sb Films. The morphology and structure of the electrodeposited Sb films with CTAB and SPS appear to be significantly altered as seen through scanning electron microscopy (SEM), Figure 3. When no additives are used in solution, Sb deposits in small bushlike structures with small branches poking out and sharp faceting as seen in the cross-section imaging in Figure 4. Upon adding 1 mM SPS, Sb begins to deposit in larger agglomerates, and as the concentration is increased to 10 mM, the agglomerates continue to increase in size. When the concentration is increased to 30 mM, the morphology changes significantly and crystallites grow in longer branches out from the current collector and, due to their weight, bend over horizontally. We hypothesize SPS could be inhibiting the nucleation of Sb ions across the surface of the copper substrate and instead promotes its growth along already nucleated areas resulting in columnar growth, as seen in the cross-section imaging, Figure 4. To determine if SPS is incorporated into the film, X-ray photoelectron spectroscopy (XPS) was conducted on two films of different loadings to identify sulfur components in the electrodeposited antimony films, Figure 5. Choe et al. found that, in copper deposition baths, SPS degrades due to a catalytic oxidation reaction with copper ions in solution.[60] Because of this, we hypothesized that sulfur could be trapped at the boundary between copper and the electrodeposited antimony. In the case of both pristine samples, no quantifiable amount of sulfur was identified at the surface of the deposit; however, the low loading/thinner film (deposited for 30 s) showed a sulfur peak after 180 s of sputtering as well as copper

https://doi.org/10.1021/acs.jpcc.3c01086
J. Phys. Chem. C 2023, 127, 12415−12427

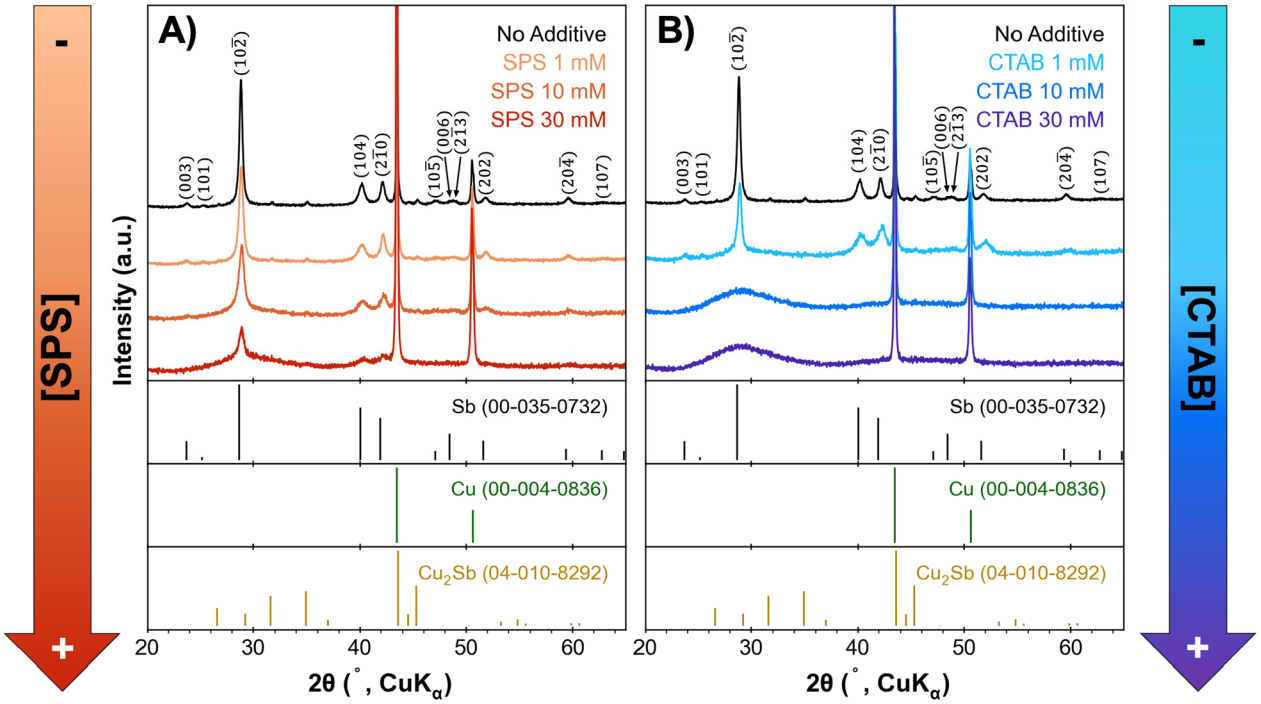

Figure 6. PXRD patterns of Sb films deposited with no additive, and varying concentrations of SPS (A) and CTAB (B). Further analysis including Rietveld refinements can be found in Figure S5.

environments related to the surface of the current collector. These results demonstrate that SPS is not significantly incorporated throughout the film, but sulfur is present on the copper substrate, which is consistent with the hypothesis that SPS adsorption limits the initial surface area on which Sb can deposit.

When CTAB was implemented into the solution the morphology of the deposited Sb had the most significant change. At a concentration of 1 mM CTAB, the agglomerates began to smooth out and increase in size. We believe the deposition forms smoother particles due to the adsorption of CTAB onto the surface of the deposited Sb which hinders the ability for more Sb to deposit on that surface. In addition, it has been reported that surfactants such as CTAB can help maintain interfacial surface tension over the deposit and can lead to compact deposits.[61] As the concentration is increased to 10 mM, the same smoothing effect is seen and is exacerbated. The film was mainly composed of large densely packed smooth particles as seen in Figure 3 and Figure 4. However, when increasing the concentration of CTAB to 30 mM, the morphology remained the same. When characterizing the composition of the film through XPS, Figure S2 and Figure S3, no components of the additive are present even after sputtering through the film. This leads us to hypothesize that CTAB binding must be reversible and could be influencing the growth of the film, but does not remain incorporated throughout the film.

To investigate if CTAB has a more significant impact on the morphology than SPS, we electrodeposited an Sb film with a combination of 30 mM CTAB and SPS. These films had a similar morphology to the 30 mM SPS, Figure S4, as characterized by the long branching, but some characteristics similar to the films deposited with CTAB were also present. In small areas of the film, CTAB behaved similarly to how it acts alone, and led to smoothing of the ends of the branches, essentially capping further growth of the deposit. However, throughout most of the film, SPS heavily dominated the deposition by encouraging columnar growth, consistent with blocking of the Cu substrate as previously described. From this deposition, it is clear that CTAB and SPS alter the deposition through separate mechanisms, as both types of modification to the morphology are observed.

Variation in the deposition of Sb induced by solution additives results in changes to film morphology, which likely means that a significant change in film structure occurs as well. Components of film structure, such as crystallite size and strain, can have a large impact on battery performance.[62−64] To further understand how the solution additives could influence the growth of the Sb deposits, PXRD and subsequent Rietveld refinements were performed, Figures 6A and B and Figures S5. PXRD peak breadth increases with an increase in additive concentration, which is indicative of changes in crystal microstructure, and either a decrease in crystallite size or increase in microstrain. The contributions of crystallite size and microstrain can be deconvoluted in refinements given sufficient intensity of high 2θ reflections, and is discussed further in the Supporting Information.[65,66]

The mean crystallite size, microstrain, lattice parameters, $(10\bar{2})$ d-spacing, and preferential orientation were calculated using Rietveld refinements (Table S1). The no additive film is the most crystalline, and does exhibit microstrain, consistent with the fact that strain is common in electrodeposited films.[22,67,68] Large crystallites of 1 mM SPS and CTAB films are similar in size at ∼70 nm, though the CTAB film also has a low crystalline Sb component, <2 nm, so overall the 1 mM CTAB film is less crystalline. The SPS films are considerably more crystalline for the remaining concentrations of additives than their CTAB counterparts, and crystallite size does not change substantially until a poorly crystalline Sb phase emerges at 30 mM SPS. In the case of CTAB, crystallinity decreases

https://doi.org/10.1021/acs.jpcc.3c01086
J. Phys. Chem. C 2023, 127, 12415−12427

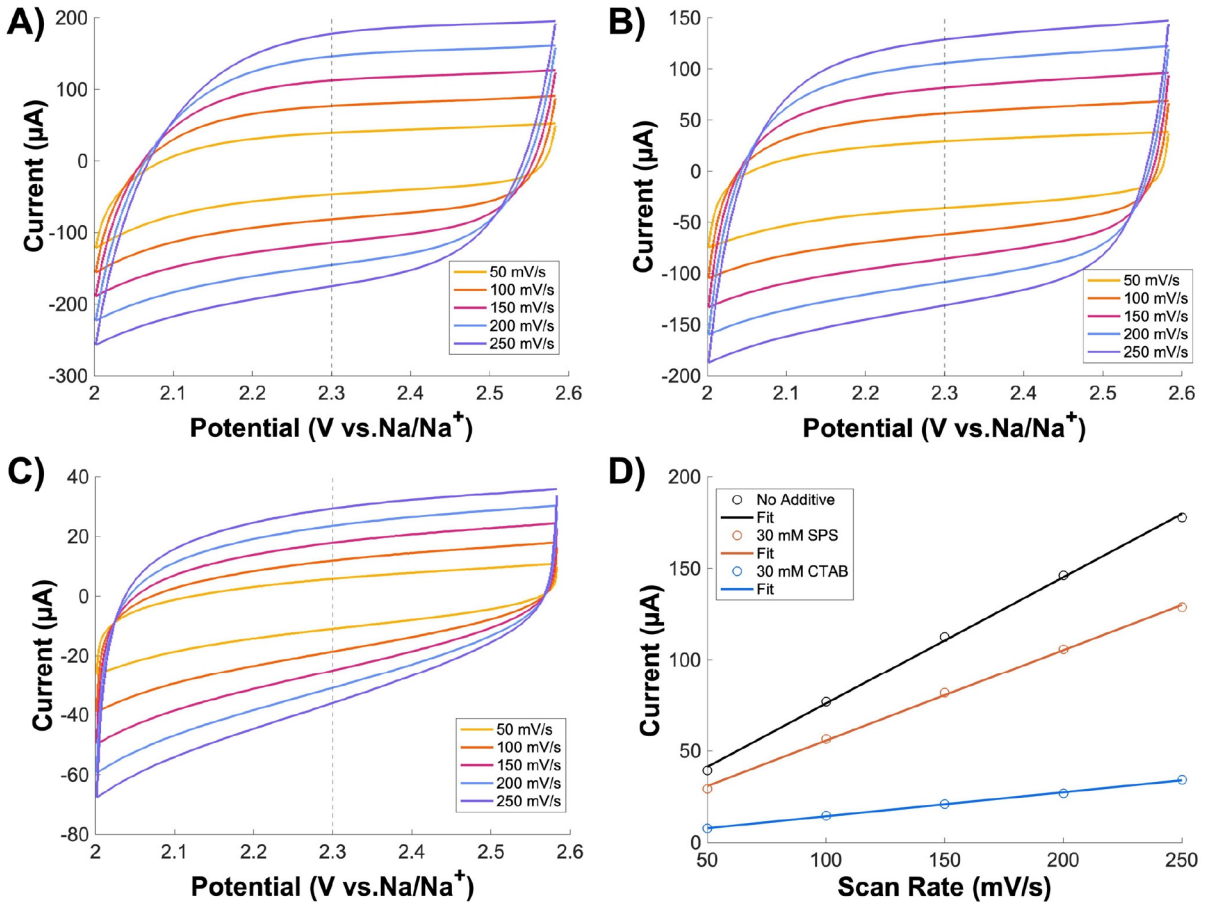

Figure 7. CV scans of Sb films deposited with (A) No additive, (B) 30 mM SPS, and (C) 30 mM CTAB. Scans were done in a three-electrode sodium battery with sodium metal as both the reference and counter electrodes in a 1 M $NaClO_4$ in PC and 5% FEC electrolyte. The cells were cycled in the potential range of 2 V−2.6 V vs Na/Na^+ at scan rates of 50, 100, 150, 200, and 250 mV/s. Scan rates were plotted against the current response at 2.3 V vs Na/Na^+ for the Sb films deposited with no additive (black), 30 mM CTAB (blue), and 30 mM SPS (orange). Values for the determined surface area of all three Sb films can be found in Table S2.

rapidly when the concentration is increased, and at 10 and 30 mM, films are nearly amorphous. This is consistent with SEM images, as SPS films appear to have visible grains; at higher CTAB concentrations, films are of such low crystallinity that grains are difficult to distinguish, and instead only large agglomerates or particles are observed. In addition, strain is considerable in the 10 and 30 mM CTAB films, observed by decreased $(10\bar{2})$ plane spacing. Preferential orientation is observed in the $[10\bar{2}]$ for most films, suggesting that this is the preferred direction of growth. In SPS films, considerable anisotropic broadening is observed, indicating strain in the [104]. Strain in this direction could be caused by the fact that this plane is nearly perpendicular to the $(10\bar{2})$, and rapid growth in the $[10\bar{2}]$ could cause strain in the perpendicular direction.[22,67,68]

In both additive systems, film crystallinity decreases and strain increases with a higher additive concentration. CTAB appears to have a more drastic effect on film microstructure for a given additive concentration. As CTAB has been shown to be a capping ligand, we propose that it acts so here, capping crystals at small sizes and passivating the film surface so that added Sb must nucleate in a new crystal, rather than incorporating into existing crystals, resulting in nearly amorphous films at high concentrations. The strain in the 10 and 30 mM CTAB films likely results from densely packed agglomerates pushing against each other as Sb deposits. In the SPS system, crystallite size is less drastically affected compared to CTAB until the emergence of the <2 nm Sb in the 30 mM SPS film, but anisotropic strain is considerable, which once again suggests that these two additives influence the nucleation and growth of the film through different mechanisms. We propose that as SPS is an accelerant, it is possible that it causes nucleation and growth to occur more rapidly, resulting in increased strain as the concentration is increased. As previously mentioned, at the high concentration of 30 mM, the SPS may have reached a sufficient concentration to remove most of the passivating layers of gluconate and/or Cl^-, as seen in other studies,[59] and nucleation could occur much more rapidly, which would explain the increased branching and drastic decrease to <2 nm crystallite sizes.

Electrochemical Characterization of Electrodeposited Sb Films. Due to the significant morphological and structural changes observed when implementing the use of solution additives, it was necessary to determine how the electrochemical properties of the deposited Sb films were altered. For example, these changes in morphology and particle size can lead to changes in the electrochemical surface area (ECSA) which is defined in this study as the exposed surface of the active electrode in contact with the electrolyte.[69] Due to microstructuring that occurs during the electrodeposition of these films, the geometric surface and ECSA are not equivalent. To determine the ECSA of the electrodeposited

https://doi.org/10.1021/acs.jpcc.3c01086
J. Phys. Chem. C 2023, 127, 12415−12427

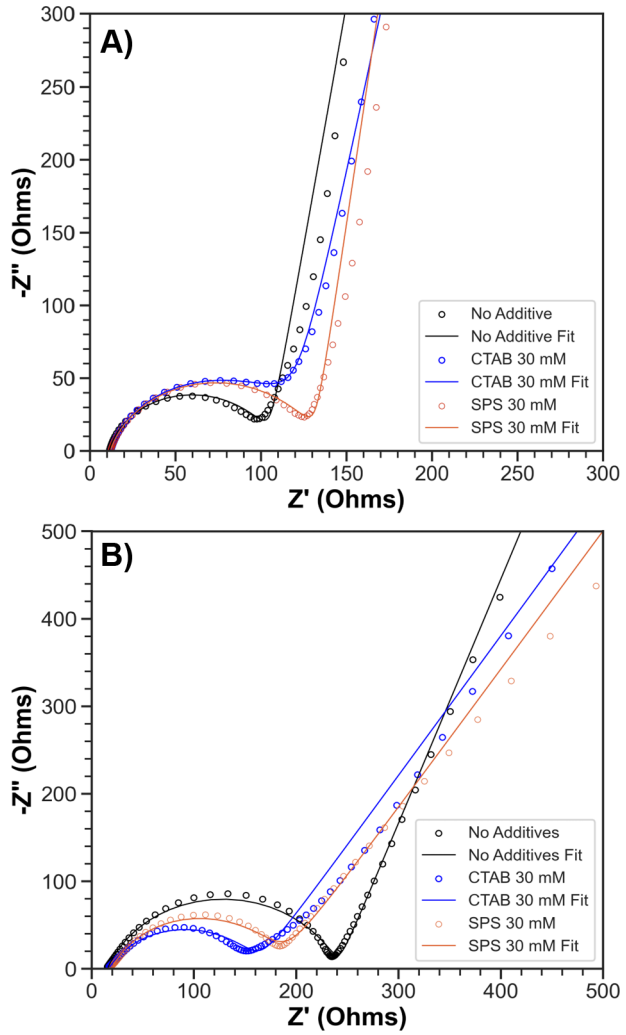

Figure 8. Nyquist plots of Sb films deposited with no additives (black), 30 mM CTAB (blue), and SPS (orange). EIS was conducted in a sodium half-cell at room temperature, on the pristine anodes at OCP (A), and after 10 cycles in a sodiated state at 0.01 V (B). The EIS data was modeled through a modified Randles circuit, Scheme S1, and values for each component previously described are quantified in Table S3.

films, similar experiments reported in the field of electrocatalysis were performed.[69,70] To measure the nonfaradaic current response and calculate the double layer capacitance, CVs were conducted in the potential range of 2 V−2.6 V vs Na/Na^+ where no sodiation/desodiation reactions of Sb should occur, Figure 7. The deposited Sb films were cycled at different scan rates, and the current response at 2.3 V vs Na/Na^+ was plotted as a function of the scan rates. The nonfaradic current scales linearly with the scan rate and can be used to determine the ECSA. A summary of the determined values is reported in Table S2, and a more in-depth explanation of the ECSA calculations as well as all ECSA values determined for Sb films deposited with no additive, 30 mM CTAB, and 30 mM SPS can be found in the Supporting Information. However, it is important to note that the ECSA encompasses all electrochemically active sites, which includes Sb_2O_3 that we observe through XPS. When comparing these results to the SEM images in Figure 3 and Figure 4, the determined ECSA values seem consistent with expected available surface area. The no additive film has the highest ECSA ($ECSA_{(No\ Additive)}$ = 9.28 ± 0.22 cm^2), due to its growth in small agglomerates across the whole film. In the 30 mM SPS film ($ECSA_{(SPS\ 30\ mM)}$ = 6.49 ± 0.09 cm^2), the ECSA was lower and the small agglomerates significantly grew in size into long branches across the film. This morphology may lead to a decrease in the ECSA due to the denser packing observed in Figure 4. The Sb film deposited with 30 mM CTAB ($ECSA_{(CTAB\ 30\ mM)}$ = 1.60 ± 0.1 cm^2) had the lowest ECSA likely due to the dense packing of the large smooth particles.

Further electrochemical characterization through electrochemical impedance spectroscopy (EIS) shows that CTAB and SPS also influence the resistivity of the deposited film. From the Nyquist plot shown in Figure 8, there are three major areas that can be compared visually. These areas are related to the ionic resistance in solution depicted by the *x*-axis offset, the charge transfer resistance depicted by width of the semicircle, and solid-state diffusion throughout the electrode shown by the Warburg tail at lower frequencies. The EIS data were modeled through a modified Randles circuit, Scheme S1, and values for each component previously described are quantified in Table S3. From these fits, Figure 8A, it was determined that Sb films deposited with no additive had the lowest charge transfer resistance (R_{ct}) at 95.95 Ω and the CTAB and SPS films had similar R_{ct} values at 120 Ω and 122.2 Ω, respectively. These results demonstrate that the use of SPS and CTAB do not significantly increase charge transfer resistance, by either minuscule inclusions of the additive or changes to grain boundaries. It is difficult to make a strong conclusion about the solid-state diffusion due to challenges in modeling this behavior in porous and alloying electrodes that has been described in the field.[71,72] To attempt to understand the Na^+ diffusion coefficient regardless of the described difficulties, EIS was performed on the no additive, SPS 30 mM, and CTAB 30 mM films after 10 cycles, Figure 8B. After 10 cycles, the R_{ct} increases for all three films with the no additive film having the highest increase from 95.95 Ω to 225.8 Ω. This increase in R_{ct} is believed to be caused by the poor mechanical stability of the no additive film, leading to loss of active material and potentially an excessive buildup of SEI as discussed when analyzing the electrochemical performance of the films. Additionally, we calculated the Warburg diffusion coefficients for Na (D_{Na}) in the Sb anodes based off of the work by Dashairya et al.,[73] Figure S6. An explanation of how the calculations were performed can be found in the Supporting Information, and the determined D_{Na} for each anode can be found in Table S4. The Warburg diffusion coefficients were calculated for the Sb anodes deposited with no additive, SPS, and CTAB, and the values were 1.51 × 10^{-18} cm^2 s^{-1}, 2.91 × 10^{-19} cm^2 s^{-1}, and 7.94 × 10^{-18} cm^2 s^{-1}, respectively. When compared to the work of Dashairya et al., our diffusion coefficients are five orders of magnitude lower. We believe our diffusion coefficients are smaller because the electrodeposited films in this study are densely packed bulk films with no carbon additives, whereas the study by Dashairya et al. investigated the properties of Sb nanoparticles that were embedded in graphite oxide sheets.[73] The smaller particle size and conductive carbon additive likely led to faster sodium diffusion throughout the electrode. Interestingly, in our study the SPS 30 mM film had a higher ECSA than the CTAB films, but it had the lowest diffusion coefficient. These results further demonstrate that other factors such as morphology and surface area could also affect the electrochemical performance.

https://doi.org/10.1021/acs.jpcc.3c01086
J. Phys. Chem. C 2023, 127, 12415−12427

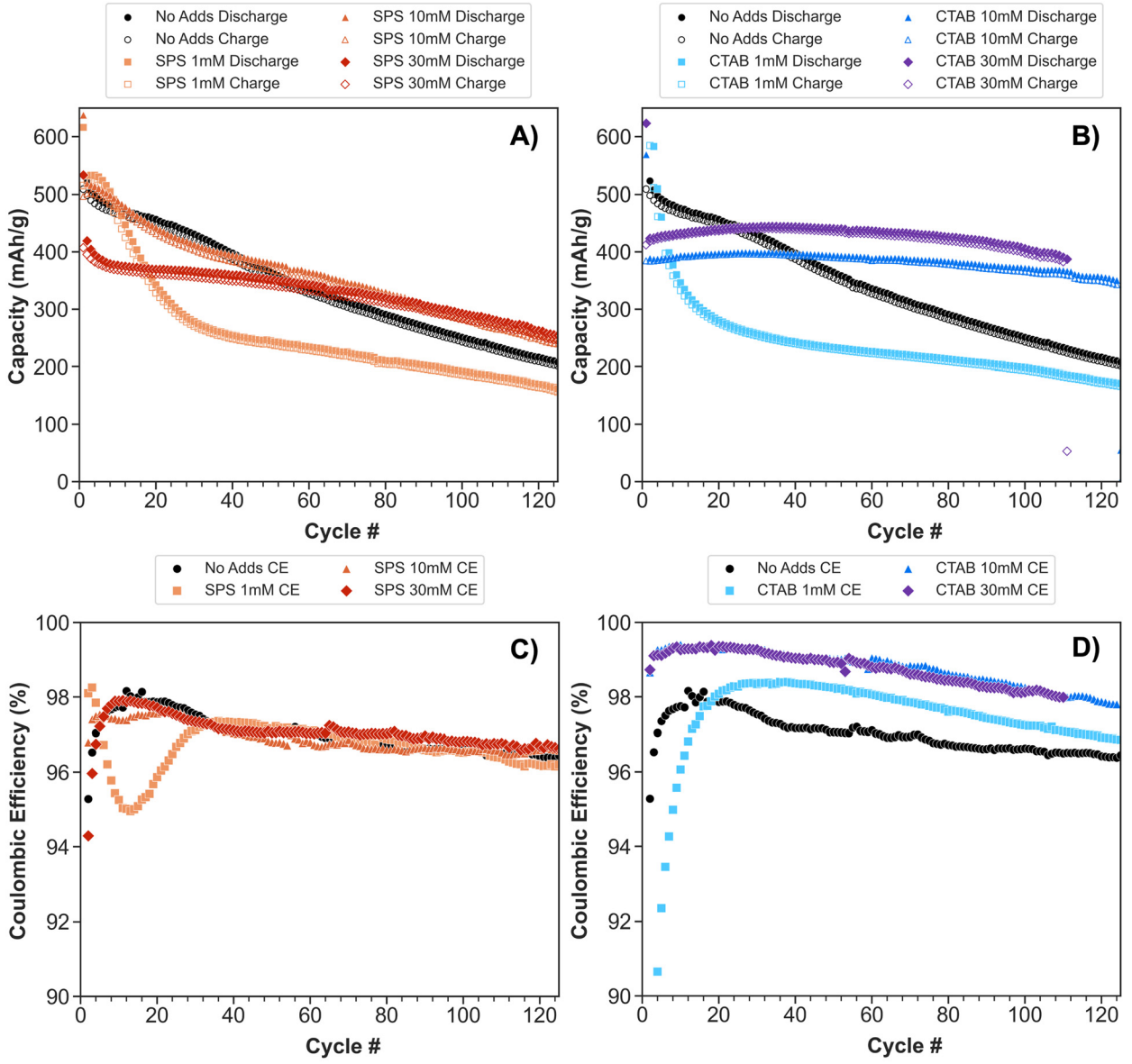

Figure 9. Cycling performance and corresponding Coulombic Efficiency (CE) of Sb films deposited with no additives, and at different concentrations of SPS (A and C) and CTAB (B and D). Tests were done in a sodium half-cell at a rate of C/2 in the potential window of 0.01 V–1.5 V vs Na/Na^+.

Electrochemical Performance of Electrodeposited Sb in Na-Ion Half-Cells. Upon comparing the electrochemical performance of the deposited films in a sodium half-cell, Figure 9, both CTAB and SPS are seen to affect cycling stability. As the concentration of SPS is increased, the capacity retention at 60 cycles slightly increases, but there are still significant decreases in capacity present for the 1 mM and 10 mM SPS films at early cycles. When the concentration is increased to 30 mM SPS, the capacity decreases and the CE is lower in the first few cycles but remains stable for 50 cycles. We hypothesize that the longer branches produced from the accelerated growth of the films prompted by SPS are more fragile and tend to pulverize upon sodiation/desodiation in early cycles as seen in ex situ post cycling SEM in Figure S7. This was further shown as active material could be rubbed off the film, characteristic of fragile dendritic growth, and when rinsing the electrode for post cycling ex situ characterization, active material was lost in the rinse, Figure S8. However, even after cycling the deposited film remained relatively intact with the copper substrate and no copper was seen through the film when compared to the no additive film. After cycling the no additive film has large areas of exposed copper, indicating that delamination and pulverization are the main modes of failure for these films, which suggests that SPS is improving the adhesion between the deposit and the substrate by preventing delamination and the mechanical integrity of the columnar like growth is the main mode of failure for these films.

Electrodepositing Sb in the presence of 10 mM and 30 mM CTAB significantly improved the capacity retention when compared to the performance of a film deposited with no additive and with SPS, Figure 9. The increase in cycling stability and Coulombic efficiencies (CE) is attributed to the improved mechanical stability as seen in post-cycling ex situ characterization, Figure S7. Upon cycling, the CTAB film experienced mechanical instability inherent to alloying electrodes but remained relatively intact as no exposed copper was

https://doi.org/10.1021/acs.jpcc.3c01086
J. Phys. Chem. C 2023, 127, 12415–12427

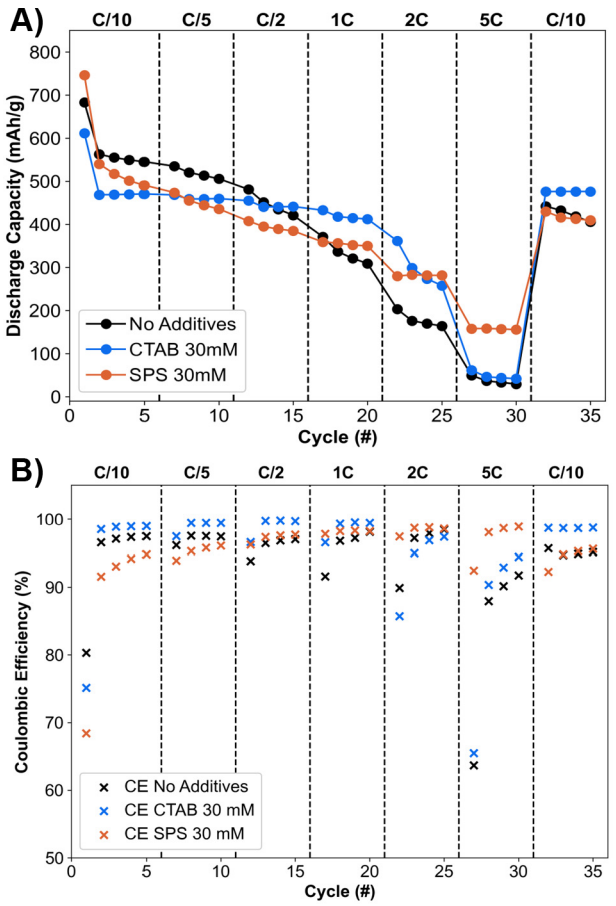

Figure 10. Discharge capacity (A) and Coulombic Efficiency (CE) (B) for rate capability tests on the Sb films deposited with no additive (black), with 30 mM CTAB (blue), and 30 mM SPS (orange). These tests were done in a sodium half-cell at 5 cycles for each rate.

seen through ex situ analysis, Figures S7 and S8. We believe the improved mechanical stability is due to the densely packed smooth particles that were well adhered to the copper substrate. In addition to the mechanical properties of the film, the 10 and 30 mM CTAB films are nearly amorphous and have smaller crystallite sizes. The amorphous nature of the CTAB films may also lead to improved mechanical stability due to the large volume expansion that crystalline Sb experiences when fully sodiated to Na_3Sb.[74,75] Therefore, the more amorphous films have better capacity retention and higher CE as seen in Figure 9. Additionally, when comparing the sodiation/desodiation reactions of the Sb anodes deposited with no additives, 30 mM CTAB, and 30 mM SPS, Figure S9, all three films experience the same sodiation/desodiation reactions further demonstrating that any incorporation of additives in the film is not active in the sodiation/desodiation process.

Rate performance tests, Figure 10A and B, demonstrate similar trends with cycling stability, as the 30 mM CTAB film still has the best capacity retention and CE when cycled at variable rates for 35 cycles. All three films experienced substantial kinetic limitations at high rates of 5C, but the SPS film managed to retain capacity at 190 mAh/g. We propose that the higher calculated ECSA for the SPS film allows for better rate capability because more exposed active material is available for sodiation/desodiation. In addition, the smaller crystallite size induced by increasing the concentration of SPS could be leading to better rate capabilities as seen by comparing the performance of all three concentrations in Figure S10. In contrast, the no additive film was found to have the highest ECSA 9.26 ± 0.2 cm^2 and based on this factor alone would be predicted to have the best rate performance. Instead, it is plagued by detrimental mechanical instability depicted by the lower CE during cycling and the continuous loss of capacity when the cell is returned to a C/10 rate. When considering solely the ECSA, the 30 mM CTAB film behaved as expected and had poor capacity retention at higher rates. Similar to the SPS films, as the crystallite size decreases with the increase in CTAB, the rate performance also improves, Figure S10. However, it is challenging to pinpoint one specific property that could explain the improved rate capabilities because the CTAB films also dramatically decreased in overall crystallinity. This decreased crystallinity of the SPS and CTAB films also contributes to slower kinetics in the sodiation/desodiation mechanism as seen in the differential capacity (dQ/dV) data, Figure S9, and is characterized by the broadening of peaks and shifts in overpotential when compared to the no additive film.

CONCLUSION

In this work, we show that the electrodeposition of Sb anodes with solution additives enables significant control and tunability of morphology and crystallinity, which in turn impacts battery performance. The addition of CTAB leads to amorphous, strained films with smooth, densely packed particles. This is likely due to CTAB inhibiting Sb deposition as growth occurs and these films have the lowest ECSA. The SPS films are more crystalline than their CTAB counterparts and exhibit columnar growth; we propose that crystallinity decreases with higher concentrations because of accelerated growth. The combination of morphological and structural changes lead to trade-offs in the electrochemical performance of these films in NIBs. Due to the mechanical robustness and better adhesion to the copper substrate brought from the influences of CTAB, these films have better capacity retention and remain relatively intact upon continuous sodiation/desodiation. However, the capacity retention diminishes at higher rates potentially due to the amorphous nature of the film. In contrast, the SPS films have a worse cycle life due to the increased fragility of the long columnar like morphology. Despite this mechanical instability, SPS films retain higher capacities at rates of 5C when compared to the CTAB and no additive films. We hypothesize that this is a result of the higher ECSA and decreased crystallite size of the deposit and the overall higher crystallinity of the film when compared to the CTAB films.

Controlling specific structural, morphological, and electrochemical properties of the electrodeposited Sb films is of great importance as it significantly impacts the overall performance in a NIB. There are significant trade-offs to consider with lifetime or rate capabilities of the cell, and one could imagine tuning these films according to what application the batteries will be used for. Overall, these studies provide insight into the integral role solution additives can play in the formation of these films, and how electrodeposition can be utilized to control material properties of alloy-based anode materials to optimize NIB performance.

https://doi.org/10.1021/acs.jpcc.3c01086
J. Phys. Chem. C 2023, 127, 12415−12427

■ ASSOCIATED CONTENT

Supporting Information

The Supporting Information is available free of charge at https://pubs.acs.org/doi/10.1021/acs.jpcc.3c01086.

Further discussion on Rietveld refinements, ECSA measurements, and EIS fitting are provided. Additionally, XPS data for Sb films deposited with 30 mM CTAB at different loadings along with SEM images post cycling of a no additive, 30 mM CTAB and 30 mM SPS films have been provided. Rate capability data on various concentrations of CTAB and SPS and dQ/dV for the rate experiments presented for the no additive, 30 mM CTAB and 30 mM SPS films are provided (PDF)

■ AUTHOR INFORMATION

Corresponding Author

Amy L. Prieto − *Department of Chemistry, Colorado State University, Fort Collins, Colorado 80523, United States;* orcid.org/0000-0001-9235-185X; Email: amy.prieto@colostate.edu

Authors

Kelly Nieto − *Department of Chemistry, Colorado State University, Fort Collins, Colorado 80523, United States;* orcid.org/0000-0002-8833-0113

Daniel S. Windsor − *Department of Chemistry, Colorado State University, Fort Collins, Colorado 80523, United States*

Amanda R. Kale − *Department of Chemistry, Colorado State University, Fort Collins, Colorado 80523, United States;* orcid.org/0000-0003-2058-902X

Jessica R. Gallawa − *Department of Chemistry, Colorado State University, Fort Collins, Colorado 80523, United States*

Dylan A. Medina − *Department of Chemistry, Colorado State University, Fort Collins, Colorado 80523, United States*

Complete contact information is available at: https://pubs.acs.org/10.1021/acs.jpcc.3c01086

Author Contributions

K.N. developed initial hypotheses, designed experiments, analyzed data, and led the writing of the manuscript. D.S.W. developed the ECSA experiments, fit impedance data, analyzed data, and assisted in writing the manuscript. A.R.K. performed and interpreted Rietveld refinements as well as assisted with hypothesis development and writing the manuscript. J.R.G. performed, fit, and analyzed the XPS data and assisted with writing the manuscript. D.A.M. assisted with the synthesis of anode material and assembly of cells. A.L.P. assisted with the conceptualization of this project, data interpretation, and manuscript editing.

Notes

The authors declare no competing financial interest.

■ ACKNOWLEDGMENTS

We are honored to submit this manuscript for inclusion in the Esther Sans Takeuchi Festschrif, honoring the work of Prof. Esther Sans Takeuchi. A.L.P. thanks Prof. Takeuchi for her leadership in the field, her ability to set high standards for herself and others, and her generous mentoring. K.N was supported in part through an American Dissertation Fellowship from the American Association of University Women (AAUW). This work was partially funded by NSF SSMC-2211067. We acknowledge the CSU Analytical Resources Core facility for the use of their instruments and facility (SCR_021758). Special thanks to the Analytical Resources Core staff at CSU, especially Dr. Rebecca Miller and Dr. Brian Newell for their help with XPS, SEM, and PXRD.

■ REFERENCES

(1) Kim, Y.; Ha, K. H.; Oh, S. M.; Lee, K. T. High-Capacity Anode Materials for Sodium-Ion Batteries. *Chem.—Eur. J.* **2014**, *20*, 11980−11992.

(2) Sarkar, S.; Peter, S. C. An Overview on Sb-Based Intermetallics and Alloys for Sodium-Ion Batteries: Trends, Challenges and Future Prospects from Material Synthesis to Battery Performance. *J. Mater. Chem. A Mater.* **2021**, *9*, 5164−5196.

(3) He, J.; Wei, Y.; Zhai, T.; Li, H. Antimony-Based Materials as Promising Anodes for Rechargeable Lithium-Ion and Sodium-Ion Batteries. *Mater. Chem. Front* **2018**, *2*, 437.

(4) Schulze, M. C.; Belson, R. M.; Kraynak, L. A.; Prieto, A. L. Electrodeposition of Sb/CNT Composite Films as Anodes for Li- and Na-Ion Batteries. *Energy Storage Mater.* **2020**, *25*, 572−584.

(5) Pfeifer, K.; Arnold, S.; Budak, Ö.; Luo, X.; Presser, V.; Ehrenberg, H.; Dsoke, S. Choosing the Right Carbon Additive Is of Vital Importance for High-Performance Sb-Based Na-Ion Batteries. *J. Mater. Chem. A Mater.* **2020**, *8*, 6092−6104.

(6) Liang, S.; Cheng, Y. J.; Zhu, J.; Xia, Y.; Müller-Buschbaum, P. A Chronicle Review of Nonsilicon (Sn, Sb, Ge)-Based Lithium/Sodium-Ion Battery Alloying Anodes. *Small Methods* **2020**, *4*, 2000218.

(7) Voigt, K.; Heubner, C.; Liebmann, T.; Matthey, B.; Weiser, M.; Schneider, M.; Michaelis, A. Electrodeposition of Versatile Nanostructured Sb/Sb_2O_3 Microcomposites: A Parameter Study. *Adv. Mater. Interfaces* **2020**, *7*, 2000004.

(8) Lv, H.; Qiu, S.; Lu, G.; Fu, Y.; Li, X.; Hu, C.; Liu, J. *Nanostructured Antimony/Carbon Composite Fibers as Anode Material for Lithium-Ion Battery* **2015**, *151*, 214−221.

(9) Nagulapati, V. M.; Yoon, Y. H.; Kim, D. S.; Kim, H.; Lee, W. S.; Lee, J. H.; Kim, K. H.; Hur, J.; Kim, I. T.; Lee, S. G. Effect of Binders and Additives to Tailor the Electrochemical Performance of Sb_2Te_3-TiC Alloy Anodes for High-Performance Sodium-Ion Batteries. *Journal of Industrial and Engineering Chemistry* **2019**, *76*, 419−428.

(10) Wenzel, V.; Nirschl, H.; Nötzel, D. Challenges in Lithium-Ion-Battery Slurry Preparation and Potential of Modifying Electrode Structures by Different Mixing Processes. *Energy Technology* **2015**, *3*, 692−698.

(11) Hays, K. A.; Armstrong, B.; Veith, G. M. Ending the Chase for a Perfect Binder: Role of Surface Chemistry Variation and Its Influence on Silicon Anodes. *ChemElectroChem.* **2020**, *7*, 3790−3797.

(12) Baggetto, L.; Ganesh, P.; Sun, C.-N.; Meisner, R. A.; Zawodzinski, T. A.; Veith, G. M. Intrinsic Thermodynamic and Kinetic Properties of Sb Electrodes for Li-Ion and Na-Ion Batteries: Experiment and Theory. *J. Mater. Chem. A Mater.* **2013**, *1*, 7985−7994.

(13) Li, Z.; Tan, X.; Li, P.; Kalisvaart, P.; Janish, M. T.; Mook, W. M.; Luber, E. J.; Jungjohann, K. L.; Carter, C. B.; Mitlin, D. Coupling In Situ TEM and Ex Situ Analysis to Understand Heterogeneous Sodiation of Antimony. *Nano Lett.* **2015**, *15*, 6339−6348.

(14) Qiu, S.; Wu, X.; Xiao, L.; Ai, X.; Yang, H.; Cao, Y. Antimony Nanocrystals Encapsulated in Carbon Microspheres Synthesized by a Facile Self-Catalyzing Solvothermal Method for High-Performance Sodium-Ion Battery Anodes. *ACS Appl. Mater. Interfaces* **2016**, *8*, 1337−1343.

(15) Zhang, Y.; Xie, J.; Zhu, T.; Cao, G.; Zhao, X.; Zhang, S. Activation of Electrochemical Lithium and Sodium Storage of Nanocrystalline Antimony by Anchoring on Graphene via a Facile in Situ Solvothermal Route. *J. Power Sources* **2014**, *247*, 204−212.

(16) Jackson, E. D.; Prieto, A. L. Copper Antimonide Nanowire Array Lithium Ion Anodes Stabilized by Electrolyte Additives. *ACS Appl. Mater. Interfaces* **2016**, *8*, 30379−30386.

(17) Ma, J.; Prieto, A. L. Electrodeposition of Pure Phase SnSb Exhibiting High Stability as a Sodium-Ion Battery Anode. *Chem. Commun.* **2019**, *55*, 6938−6941.
(18) Mosby, J. M.; Prieto, A. L. Direct Electrodeposition of Cu_2Sb for Lithium-Ion Battery Anodes. *J. Am. Chem. Soc.* **2008**, *130*, 10656−10661.
(19) Jackson, E. D.; Green, S.; Prieto, A. L. Electrochemical Performance of Electrodeposited Zn_4 Sb_3 Films for Sodium-Ion Secondary Battery Anodes. *ACS Appl. Mater. Interfaces* **2015**, *7*, 7447−7450.
(20) Gimble, N. J.; Nieto, K.; Prieto, A. L. Electrodeposition as a Powerful Tool for the Fabrication and Characterization of Next-Generation Anodes for Sodium Ion Rechargeable Batteries. *Electrochemical Society Interface* **2021**, *30*, 59−63.
(21) Zangari, G. Electrodeposition of Alloys and Compounds in the Era of Microelectronics and Energy Conversion Technology. *Coatings* **2015**, *5*, 195−218.
(22) Nieto, K.; Gimble, N. J.; Rudolph, L. J.; Kale, A. R.; Prieto, A. L. Electrodeposition vs Slurry Casting: How Fabrication Affects Electrochemical Reactions of Sb Electrodes in Sodium-Ion Batteries. *J. Electrochem. Soc.* **2022**, *169*, No. 050537.
(23) Hong, K.-S.; Nam, D.-H.; Lim, S.-J.; Sohn, D.; Kim, T.-H.; Kwon, H. Electrochemically Synthesized Sb/Sb_2O_3 Composites as High-Capacity Anode Materials Utilizing a Reversible Conversion Reaction for Na-Ion Batteries. *ACS Appl. Mater. Interfaces* **2015**, *7*, 17264−17271.
(24) Ngo, T. T.; Chavhan, S.; Kosta, I.; Miguel, O.; Grande, H. J.; Tena-Zaera, R. Electrodeposition of Antimony Selenide Thin Films and Application in Semiconductor Sensitized Solar Cells. *ACS Appl. Mater. Interfaces* **2014**, *6*, 2836−2841.
(25) Liu, Z.; Cheng, J.; Höfft, O.; Endres, F. In Situ XPS Study of Template-Free Electrodeposition of Antimony Nanowires from an Ionic Liquid. *J. Solid State Electrochem.* **2023**, *27*, 371−378.
(26) Leimkühler, G.; Kerkamm, I.; Reineke-Koch, R. Electrodeposition of Antimony Telluride. *J. Electrochem. Soc.* **2002**, *149*, C474.
(27) Gamburg, Y. D.; Zangari, G. *Theory and Practice of Metal Electrodeposition*; Springer: New York, NY, 2011. DOI: 10.1007/978-1-4419-9669-5.
(28) Liu, W.; Yang, T. Z.; Zhou, Q. H.; Zhang, D. C.; Lei, C. M. Electrodeposition of Sb(III) in Alkaline Solutions Containing Xylitol. *Transactions of Nonferrous Metals Society of China (English Edition)* **2012**, *22* (4), 949−957.
(29) Majidzade, V. A.; Guliyev, P. H.; Aliyev, A. S.; Elrouby, M.; Tagiyev, D. B. Electrochemical Characterization and Electrode Kinetics for Antimony Electrodeposition from Its Oxychloride Solution in the Presence of Tartaric Acid. *J. Mol. Struct.* **2017**, *1136*, 7−13.
(30) Yang, M. H.; Sun, I. W. Electrodeposition of Antimony in a Water-Stable 1-Ethyl-3-Methylimidazolium Chloride Tetrafluoroborate Room Temperature Ionic Liquid. *J. Appl. Electrochem.* **2003**, *33*, 1077−1084.
(31) Sadana, Y. N.; Singh, J. P.; Kumar, R. Electrodeposition of Antimony and Antimony Alloys- A Review. *Surface Technology* **1985**, *24*, 319−353.
(32) Ghosh, J. C.; Kappana, A. N. Electrodeposition of Antimony. *J. Phys. Chem. C* **1924**, *28*, 149−160.
(33) Li, F.-H.; Wang, W.; Gao, J.-P.; Wang, S.-Y. Electrochemical Reduction Process of Sb(III) on Au Electrode Investigated by CV and EIS. *J. Electrochem. Soc.* **2009**, *156*, D84.
(34) Fan, X.-Y.; Han, J.; Jiang, Y.; Ni, J.; Gou, L.; Li, D.-L.; Li, L. Hierarchical Porous Sb Films on 3D Cu Substrate Have Promise for Stable Sodium Storage. *Applied Energy Material* **2018**, *1*, 3598−3602.
(35) Aroyo, M. Theoretical and Practical Aspects of Electrodeposition of Metal Coatings with Improved Properties (Part 1). *Plating and Surface Finishing* **1998**, *85*, 69−76.
(36) Schmitz, E. P. S.; Quinaia, S. P.; Garcia, J. R.; de Andrade, C. K.; Lopes, M. C. Influence of Commercial Organic Additives on the Nickel Electroplating. *Int. J. Electrochem Sci.* **2016**, *11*, 983−997.
(37) Aroyo, M. S. Leveling in Pulse Plating with Brighteners: Synergistic Effect of Frequency and Hydrodynamically Active Additives. *Plating and Surface Finishing* **1995**, *82*, 53−57.
(38) Moffat, T. P.; Wheeler, D.; Josell, D. Electrodeposition of Copper in the SPS-PEG-Cl Additive System. *J. Electrochem. Soc.* **2004**, *151*, C262.
(39) Vereecken, P. M.; Deligianni, H.; Binstead, R. A. The Role of SPS in Damascene Copper Electroplating. *IBM J. Res. Dev* **2005**, *49*, 3−18.
(40) Willey, M. J.; West, A. C. SPS Adsorption and Desorption during Copper Electrodeposition and Its Impact on PEG Adsorption. *J. Electrochem. Soc.* **2007**, *154*, D156.
(41) Rudnik, E.; Wojnicki, M.; Włoch, G. Effect of Gluconate Addition on the Electrodeposition of Nickel from Acidic Baths. *Surf. Coat. Technol.* **2012**, *207*, 375−388.
(42) Chat-Wilk, K.; Rudnik, E.; Włoch, G.; Osuch, P. Importance of Anions in Electrodeposition of Nickel from Gluconate Solutions. *Ionics* **2021**, *27*, 4393−4408.
(43) Lallemand, F.; Ricq, L.; Berçot, P.; Pagetti, J. Effects of Organic Additives on Electroplated Iron-Group Metals and Alloys. *Surf. Coat. Technol.* **1998**, *44*, 2886.
(44) Sciscenko, I.; Pedre, I.; Hunt, A.; Bogo, H.; González, G. A. Determination of a Typical Additive in Zinc Electroplating Baths. *Microchemical Journal* **2016**, *127*, 226−230.
(45) Maharana, H. S.; Basu, A.; Mondal, K. Effect of CTAB on the Architecture and Hydrophobicity of Electrodeposited $Cu−ZrO_2$ Nano-Cone Arrays. *Surf. Coat. Technol.* **2019**, *375*, 323−333.
(46) Chen, Y. C.; Kuo, S. L.; Lee, J. L.; Ke, S. T.; Wong, C. H.; Ger, M. der. The Influence of Surfactant CTAB on the Microstructure and Material Properties of Nickel Microelectroforming. *Key Eng. Mater.* **2007**, *364-366*, 346−350.
(47) Rudnik, E.; Burzyńska, L.; Dolasiński, Ł.; Misiak, M. Electrodeposition of Nickel/SiC Composites in the Presence of Cetyltrimethylammonium Bromide. *Appl. Surf. Sci.* **2010**, *256* (24), 7414−7420.
(48) Maharana, H. S.; Basu, A. Evolution and Structure-Property Correlation of CTAB Assisted High Hardness Electrodeposited Cu-ZrO_2 Nano-Cone Arrays. *Surf. Coat. Technol.* **2017**, *310*, 148−156.
(49) Maharana, H. S.; Basu, A.; Mondal, K. Effect of CTAB on the Architecture and Hydrophobicity of Electrodeposited Cu−ZrO2 Nano-Cone Arrays. *Surf. Coat. Technol.* **2019**, *375*, 323−333.
(50) Fenger, R.; Fertitta, E.; Kirmse, H.; Thünemann, A. F.; Rademann, K. Size Dependent Catalysis with CTAB-Stabilized Gold Nanoparticles. *Phys. Chem. Chem. Phys.* **2012**, *14*, 9343−9349.
(51) Smith, D. K.; Korgel, B. A. The Importance of the CTAB Surfactant on the Colloidal Seed-Mediated Synthesis of Gold Nanorods. *Langmuir* **2008**, *24*, 644−649.
(52) Heuer-Jungemann, A.; Feliu, N.; Bakaimi, I.; Hamaly, M.; Alkilany, A.; Chakraborty, I.; Masood, A.; Casula, M. F.; Kostopoulou, A.; Oh, E.; et al. The Role of Ligands in the Chemical Synthesis and Applications of Inorganic Nanoparticles. *Chem. Rev.* **2019**, *119*, 4819−4880.
(53) Jennane, J.; Ebn Touhami, M.; Zehra, S.; Baymou, Y.; Kim, S. H.; Chung, I. M.; Lgaz, H. Influence of Sodium Gluconate and Cetyltrimethylammonium Bromide on the Corrosion Behavior of Duplex (α-β) Brass in Sulfuric Acid Solution. *Mater. Chem. Phys.* **2019**, *227*, 200−210.
(54) Liang, L.; Xu, Y.; Li, Y.; Dong, H.; Zhou, M.; Zhao, H.; Kaiser, U.; Lei, Y. Facile Synthesis of Hierarchical Fern Leaf-like Sb and Its Application as an Additive-Free Anode for Fast Reversible Na-Ion Storage. *J. Mater. Chem. A Mater.* **2017**, *5*, 1749−1755.
(55) Fairley, N.; Fernandez, V.; Richard-Plouet, M.; Guillot-Deudon, C.; Walton, J.; Smith, E.; Flahaut, D.; Greiner, M.; Biesinger, M.; Tougaard, S.; Morgan, D.; Baltrusaitis, J. Systematic and Collaborative Approach to Problem Solving Using X-Ray Photoelectron Spectroscopy. *Applied Surface Science Advances* **2021**, *5*, No. 100112.
(56) Moulder, J. F.; Stickle, W. F.; Sobol, P. E.; Bomben, K. D. In *Handbook of X-Ray Photoelectron Spectroscopy: A Reference Book of*

Standard Spectra for Identification and Interpretation of XPS Data; Chastain, J., Ed.; Perkin-Elmer Corporation, Waltham, 1992.
(57) Kuruvilla, A.; Francis, M.; Sudheer, K. S.; Lakshmi, M. Replacement of Sulphur with Selenium in Antimony Sulphide Thin Films. *Bulletin of Materials Science* **2022**, *45*. DOI: 10.1007/s12034-021-02651-8.
(58) Sawyer, D. T. Metal-Gluconate Complexes. *Chem. Rev.* **1964**, *64*, 633−643.
(59) Moffat, T. P.; Wheeler, D.; Josell, D. Electrodeposition of Copper in the SPS-PEG-Cl Additive System. *J. Electrochem. Soc.* **2004**, *151*, C262.
(60) Choe, S.; Kim, M. J.; Kim, H. C.; Cho, S. K.; Ahn, S. H.; Kim, S.-K.; Kim, J. J. Degradation of Bis(3-Sulfopropyl) Disulfide and Its Influence on Copper Electrodeposition for Feature Filling. *J. Electrochem. Soc.* **2013**, *160*, D3179−D3185.
(61) Ghaemi, M.; Khosravi-Fard, L.; Neshati, J. Improved Performance of Rechargeable Alkaline Batteries via Surfactant-Mediated Electrosynthesis of MnO_2. *J. Power Sources* **2005**, *141*, 340−350.
(62) Al-Tabbakh, A. A.; Karatepe, N.; Al-Zubaidi, A. B.; Benchaabane, A.; Mahmood, N. B. Crystallite Size and Lattice Strain of Lithiated Spinel Material for Rechargeable Battery by X-Ray Diffraction Peak-Broadening Analysis. *Int. J. Energy Res.* **2019**, *43*, 1903−1911.
(63) Domi, Y.; Usui, H.; Sugimoto, K.; Sakaguchi, H. Effect of Silicon Crystallite Size on Its Electrochemical Performance for Lithium-Ion Batteries. *Energy Technology* **2019**, *7*, No. 1800946.
(64) Biswal, A.; Panda, P. K.; Acharya, A. N.; Mohapatra, S.; Swain, N.; Tripathy, B. C.; Jiang, Z. T.; Minakshi Sundaram, M. Role of Additives in Electrochemical Deposition of Ternary Metal Oxide Microspheres for Supercapacitor Applications. *ACS Omega* **2020**, *5*, 3405−3417.
(65) Balzar, D.; Audebrand, N.; Daymond, M. R.; Fitch, A.; Hewat, A.; Langford, J. I.; Le Bail, A.; Louër, D.; Masson, O.; McCowan, C. N.; et al. Size-Strain Line-Broadening Analysis of the Ceria Round-Robin Sample. *J. Appl. Crystallogr.* **2004**, *37*, 911−924.
(66) Ectors, D.; Goetz-Neunhoeffer, F.; Neubauer, J. Routine (an)Isotropic Crystallite Size Analysis in the Double-Voigt Approximation Done Right? *Powder Diffr* **2017**, *32*, S27−S34.
(67) Pereira, R.; Camargo, P. C.; de Oliveira, A. J. A.; Pereira, E. C. Modulation of the Morphology, Microstructural and Magnetic Properties on Electrodeposited NiFeCu Alloys. *Surf. Coat. Technol.* **2017**, *311*, 274−281.
(68) Bouzit, F. Z.; Nemamcha, A.; Moumeni, H.; Rehspringer, J. L. Morphology and Rietveld Analysis of Nanostructured Co-Ni Electrodeposited Thin Films Obtained at Different Current Densities. *Surf. Coat. Technol.* **2017**, *315*, 172−180.
(69) Voiry, D.; Chhowalla, M.; Gogotsi, Y.; Kotov, N. A.; Li, Y.; Penner, R. M.; Schaak, R. E.; Weiss, P. S. Best Practices for Reporting Electrocatalytic Performance of Nanomaterials. *ACS Nano* **2018**, *12*, 9635−9638.
(70) Wolfe, K. D.; Dervishogullari, D.; Stachurski, C. D.; Passantino, J. M.; Kane Jennings, G.; Cliffel, D. E. Photosystem I Multilayers within Porous Indium Tin Oxide Cathodes Enhance Mediated Electron Transfer. *ChemElectroChem.* **2020**, *7*, 596.
(71) Williamson, G. A.; Hu, V. W.; Yoo, T. B.; Affandy, M.; Opie, C.; Paradis, E. K.; Holmberg, V. C. *Temperature-Dependent Electrochemical Characteristics of Antimony Nanocrystal Alloying Electrodes for Na-Ion Batteries* **2019**, *2*, 6741.
(72) Cooper, S. J.; Bertei, A.; Finegan, D. P.; Brandon, N. P. Simulated Impedance of Diffusion in Porous Media. *Electrochim. Acta* **2017**, *251*, 681−689.
(73) Dashairya, L.; Das, D.; Saha, P. Binder-Free Electrophoretic Deposition of Sb/RGO on Cu Foil for Superior Electrochemical Performance in Li-Ion and Na-Ion Batteries. *Electrochim. Acta* **2020**, *358*, No. 136948.
(74) Darwiche, A.; Marino, C.; Sougrati, M. T.; Fraisse, B.; Stievano, L.; Monconduit, L. Better Cycling Performances of Bulk Sb in Na-Ion Batteries Compared to Li-Ion Systems: An Unexpected Electrochemical Mechanism. *J. Am. Chem. Soc.* **2012**, *134*, 20805−20811.
(75) Allan, P. K.; Griffin, J. M.; Darwiche, A.; Borkiewicz, O. J.; Wiaderek, K. M.; Chapman, K. W.; Morris, A. J.; Chupas, P. J.; Monconduit, L.; Grey, C. P. Tracking Sodium-Antimonide Phase Transformations in Sodium-Ion Anodes: Insights from Operando Pair Distribution Function Analysis and Solid-State NMR Spectroscopy. *J. Am. Chem. Soc.* **2016**, *138*, 2352−2365.

https://doi.org/10.1021/acs.jpcc.3c01086
J. Phys. Chem. C 2023, 127, 12415−12427